

# Chapter 4

## Actuation and Detection of Magnetic Microparticles in a Bioanalytical Microsystem with Integrated CMOS Chip

Ulrike Lehmann, Maximilian Sergio, Emile P. Dupont, Estelle Labonne, Cristiano Niclass, Edoardo Charbon, and Martin A.M. Gijs

### Introduction

We present in this chapter some key technologies for lab-on-a-chip (LOC) applications, in particular related to magnetic transport and optical detection. Our objective is to show how these technologies can be realized and operate synergistically to support integrated biodetection.

Magnetic microparticles (“beads”) have proven to be versatile and reliable objects in biomedical analysis and are steadily gaining interest in benchtop analytical procedures as well as in miniaturized LOC systems [1–3]. The use of micrometric particles in bioassays offers the advantage of a large specific surface for chemical binding, in combination with a high mobility imposed by the long-range magnetic forces acting on the beads. Moreover the decreasing size of LOC systems enables working with single magnetic microparticles to capture a very low number of target molecules, which evidently poses the challenge of highly sensitive detection schemes.

In this chapter, we present a hybrid microsystem that combines magnetic actuation with in situ optical detection. The chosen detection mechanism allows the observation and measurement of single magnetic microparticles of different sizes, as well as the detection of fluorescent labels attached to the particles’ surface. We are able to detect mouse IgG as target antigen in a sandwich immunoassay down to a concentration of 0.1 ng/ml. Our work represents a first step toward a full diagnostic LOC system for detection of specific antigens.

### Magnetic Microparticles and Magnetic Actuation

Most magnetic microparticles are made of magnetic nanocrystals enclosed in a matrix of inert and biocompatible material such as polymer or silicon dioxide

---

Martin A.M. Gijs (✉)  
EPFL – Swiss Federal Institute of Technology, Lausanne, Switzerland

[4–6]. The nanocrystals can be composed of iron oxide (maghemite or magnetite), amalgams of transition metals (Ni, Fe, Co, Mg, or Zn), or rare earth materials (NdFeB or SmCo). Depending on the interaction of the solid material with an external magnetic field, various types of magnetism can be distinguished, such as diamagnetism, paramagnetism, ferromagnetism, antiferromagnetism, and ferrimagnetism, but since magnetic microparticles should react strongly to an applied magnetic field, a high relative susceptibility  $\chi_r$  is advantageous. For this reason, most magnetically responsive particles contain ferro- or ferrimagnetic material, such as maghemite or magnetite. Due to the small size of the enclosed magnetic nanocrystals, thermally induced fluctuations of the direction of magnetization cause the time-averaged magnetic moment of such nanocrystals to be zero in the absence of an external magnetic field and the bead becomes superparamagnetic [7]. In the presence of an external magnetic field, however, the magnetic moments of the crystallites tend to align with the field lines, expressing a relative magnetic susceptibility that is in the range of  $\chi_r \sim 10^{-2} - 10^2$ , depending on the size and the exact composition of the magnetic particle.

A superparamagnetic particle that is suspended in a liquid and is being pulled by a magnetic force experiences a set of forces, as schematically presented in Fig. 4.1. For microscopic particles, the gravitational and buoyancy forces are very small and can usually be neglected. As a consequence, the manipulation of magnetic particles in liquids is mainly guided by the two remaining diametrically opposed forces: the magnetic force that pulls on the magnetic particles and the liquid friction or drag that acts against the pull. For a moving particle in the stationary regime, we obtain

$$\vec{F}_{\text{mag}} = -\vec{F}_{\text{friction}}. \quad (4.1)$$

The magnetic force  $\vec{F}_{\text{mag}}$  on a pointlike magnetic dipole can hereby generally be expressed as [8]

$$\vec{F}_{\text{mag}} = \left( \vec{m}_p \cdot \nabla \right) \vec{B}, \quad (4.2)$$

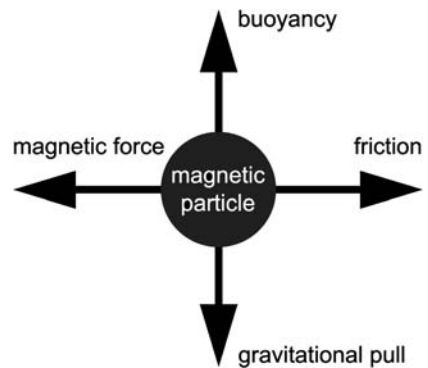


**Fig. 4.1** Diagram of the forces acting on a magnetic particle in a liquid subjected to a magnetic force perpendicular to the direction of gravitation

with  $\vec{m}_p$  the magnetic moment of the dipole and  $\vec{\nabla}\vec{B}$  the gradient of the magnetic flux density. We see from (4.2) that a nonhomogeneous magnetic field is required to obtain a translational magnetic force on the particle.

The character of the opposing liquid drag force is determined by the Reynold's number, which describes whether the flow conditions are laminar or turbulent. The limit is defined by the critical Reynold's number  $R_{\text{crit}}$ , which for water becomes  $R_{\text{crit}} \approx 2100$ . Due to the microfluidic systems' small size, the Reynold's number usually is much smaller than one, which puts the microsystem into the regime of Stokes flow, where viscous effects are larger than inertial forces. Therefore, the viscous drag force  $\vec{F}_{\text{drag}}$  in that regime follows Stokes's law [9]:

$$\vec{F}_{\text{drag}} = -3\pi D_h \eta \vec{v}_s, \quad (4.3)$$

with  $\vec{v}_s$  the mean velocity difference between liquid and particle,  $D_h$  the hydraulic diameter of the moving particle, and  $\eta$  the fluid's dynamic viscosity. The hydraulic diameter of the particle is expressed via

$$D_h = \frac{4A}{U}, \quad (4.4)$$

with  $A$  the cross sectional area and  $U$  the wetted perimeter of the cross-section.

Since the magnetic particles used in our experiments are superparamagnetic, their magnetic moment  $\vec{m}_p$ , for a field strength below saturation, can be expressed as follows:

$$\vec{m}_p = \int \Delta\chi \vec{H} dV_m, \quad (4.5)$$

with  $\Delta\chi$  the difference in relative magnetic susceptibility between the magnetic material and the surrounding medium,  $V_m$  the volume of magnetic material per microparticle, and  $\vec{H}$  the magnetic field. Equation (4.5) indicates the strong influence of a static magnetic field on the magnetization and thus on the magnetic force (4.2). When assuming a homogeneous susceptibility of the magnetic material over the volume  $V_m$ , (4.5) can be simplified and (4.2) transforms into

$$\vec{F}_{\text{mag}} = \Delta\chi V_m (\vec{H} \nabla) \vec{B} = \frac{1}{2\mu_0} \Delta\chi V_m \nabla \vec{B}^2. \quad (4.6)$$

The right-hand term is obtained via the application of the rules for the nabla operator  $\nabla$ .

Based on (4.1) and (4.3), we can therefore express the velocity  $\vec{v}_s$  of a magnetic particle as a function of the applied flux density  $\vec{B}$  or the magnetophoretic driving force  $\vec{S} \equiv \frac{\nabla B}{2\mu_0}$ .

$$\vec{v}_s = \frac{1}{3\pi} \frac{\Delta\chi V_m}{\eta D_h} \frac{\nabla \vec{B}^2}{2\mu_0} = \frac{1}{3\pi} \frac{\Delta\chi V_m}{\eta D_h} \vec{S}. \quad (4.7)$$

The proportionality factor between particle velocity  $\vec{v}_s$  and the magnetophoretic driving force  $\vec{S}$  determines the magnetophoretic mobility  $m_s$  (a “normalized” parameter analogous to the electrophoretic mobility) of a magnetic microparticle, which depends only on properties of the particle and the surrounding medium:

$$m_s = \frac{1}{3\pi} \frac{\Delta\chi V_m}{\eta D_h}. \quad (4.8)$$

The above equation shows that particles of different sizes, whose susceptibilities differ, can express the same magnetophoretic mobility. Thus, when separating and transporting magnetic particles, neither their geometry nor their magnetic properties but a combined parameter, namely, their magnetophoretic mobility, is the relevant physical quantity.

## System Setup

The magnetic manipulation system that is the focus of this chapter is based on a CMOS chip, which integrates a multilayer of microcoils with optical detection elements [10–12]. The combination of magnetic actuation and optical detection is advantageous for two reasons. Magnetic actuation offers long-range and large forces, while optical detection permits measurements of high sensitivity supported by the absence of interaction with the actuating principle. As a consequence, the manipulation and detection of single particles will be possible, which is of increasing interest for miniaturized bioanalysis. Additionally, the optical detection elements chosen on the CMOS chip enable performing on-chip fluorescent measurements, which will further enlarge the applicability of the proposed system.

The CMOS chip (Fig. 4.2) contains four metal layers, with the upper two forming the overlapping square coils, fabricated in 0.35- $\mu\text{m}$  2P4M CMOS technology. The coil double layer is responsible for the actuation of the magnetic microparticles contained in the microfluidic network placed on top of the CMOS chip. Underneath the square opening in the center of each coil, a single photon avalanche diode (SPAD) [13] is positioned, thus making the coil centers the optical detection sites.

The magnetic transport follows a three-phase current scheme [14], where an attractive coil is flanked by repulsive coils. The resulting magnetic field gradient creates a force that is sufficiently large for moving a magnetized particle to the center of the nearest attractive coil, as depicted in Fig. 4.3 [10]. In the first step, the particles are assembled around the center of the attractive coil. In the subsequent step, a neighboring coil is also changed to the attractive state, which leads to a widened but lowered magnetic field maximum, resulting in a spreading of the particle cloud over a larger area. In the third step, the first coil is changed to the repulsive state, resulting in an assembly of the magnetic particles over the neighboring, now solely attractive, coil. The optical observation of the moving cloud of particles shows that the particles follow a multitude of paths between the two coil centers, with the majority

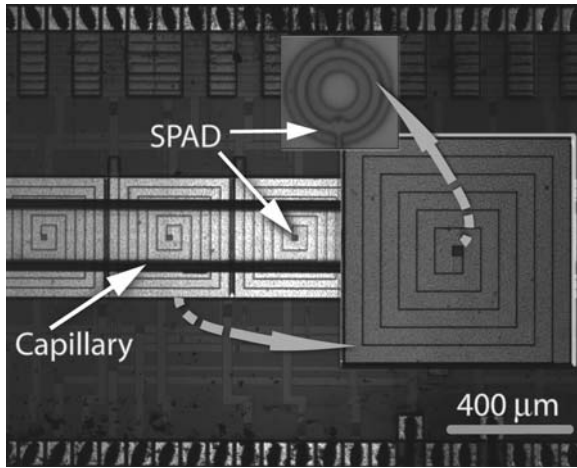


**Fig. 4.2** Photograph of the CMOS-based magnetic particle manipulation system with integrated optical detection elements [single photon avalanche diodes (SPADs)]. The insets show a coil and a SPAD in greater detail. (Reprinted from Lehmann et al. [10], with permission © 2008 Elsevier)

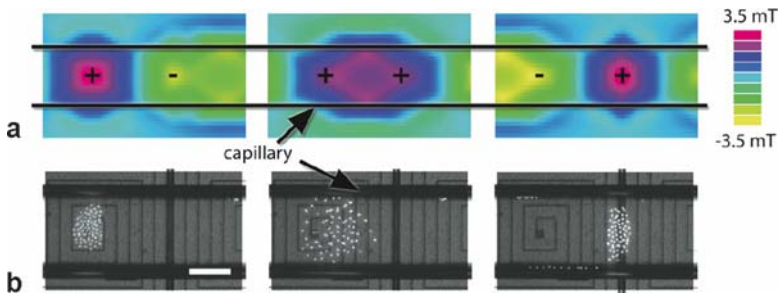


**Fig. 4.3** Magnetic particle transport. **a** Simulation of the magnetic field generated by the CMOS. The “plus” sign demonstrates a coil in attractive mode while “minus” denotes a coil in repulsive state. **b** Behavior of a group of magnetic particles 5 μm in diameter according to the respective topology of the magnetic field (dimension bar 100 μm). (Reprinted from Lehmann et al. [10], with permission © 2008 Elsevier)

moving along a straight line. Thus the path a particle describes between the two coil centers depends on its position at the coil’s center opening upon departure.

For the integrated optical detection, SPADs are chosen due to their high sensitivity, very good signal-to-noise ratio, and wide dynamic range. A SPAD is basically a *p-n* junction that is reverse biased above breakdown by the excess bias voltage  $V_e$ . Thus, for a SPAD in Geiger mode, every electron-creating event will trigger an avalanche and subsequently generate a countable signal. To achieve this, the voltage pulse generated during a detection cycle is regenerated and converted into a digital pulse by an inverter. Figure 4.4 shows a schematic of the SPAD and its surrounding circuit [10]. The diameter of the active region (anode) is in this case  $\varnothing = 8.4 \mu\text{m}$ .

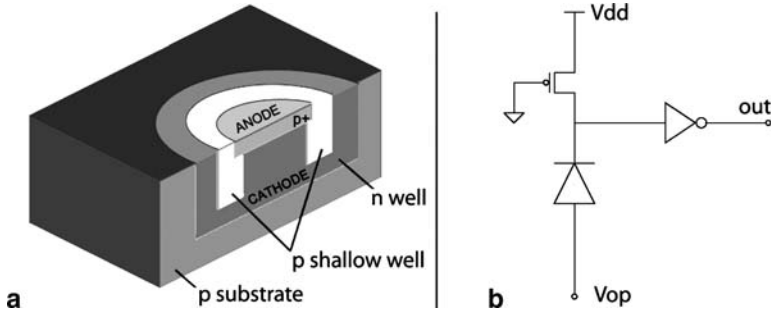


**Fig. 4.4** Schematics of the single photon avalanche diode (SPAD). **a** 3D visualization of CMOS structure. **b** Electrical circuit for SPAD in Geiger mode. (Reprinted from Lehmann et al. [10], with permission © 2008 Elsevier)

In case an avalanche is triggered in this region, the resistance placed in series to the  $p-n$  junction lets the reverse bias temporarily drop below breakdown and thus quenches the avalanche.

In our design, avalanche quenching, which in combination with the recharge time determines the dead time and thus the detection cycle of a SPAD, is achieved through a passive method. The measured dead time of 40 ns results in a maximum detectable frequency of 25 MHz. Thus an incident flux of  $25 \times 10^6$  photons per second can be detected by the SPAD.

## Optical Detection Principle

The evaluation of the signal obtained from the SPAD is based on a technique known from astronomy, where transit photometry is applied to detect and characterize extrasolar planets. This measurement principle allows the evaluation of the transiting object's properties, such as its size and the composition of its atmosphere via optical effects. In the present case, the dimensions are significantly smaller, but the ratios and observed effects are comparable. Figure 4.5a, b presents the events expected during a particle's transit. Due to the numerical aperture of the microscope's objective and the circular detection area, the light source appears as a large disc. Any particle passing between the SPAD and the light source will block a fraction of the incoming light, therefore creating a transiting dark spot or "microeclipse." Such events are known from astronomy, when planets pass between an earthbound telescope and the sun or between an observing satellite and a distant star, as shown in Fig. 4.5c. Transit photometry exploits the fact that the passage of an object (radius  $r$ ) in front of a light source (radius  $R \gg r$ ) results in a lowered light intensity measured at a detector directed toward the respective light source. Thus, the photon count of a SPAD drops during the passage of a magnetic particle between the active area and the microscope's light source.

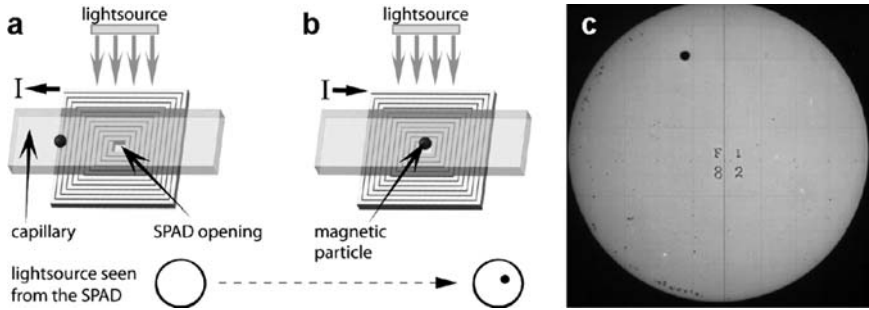


**Fig. 4.5** Principle of microeclipse detection. **a** In the absence of a particle, the single photon avalanche diode (SPAD) is fully illuminated. **b** In the presence of a particle over the SPAD, the incident light is partly obstructed. **c** Transit of planet Venus on 6 December 1882. This picture, taken by American transit-expedition, is probably the oldest photograph of Venus

## Experimental Results

### *Magnetic Particle Transport*

A first range of experiments is performed in order to study the system's behavior with respect to the magnetic transport and optical detection capabilities. Magnetic particles 30  $\mu\text{m}$  in diameter (Micromod) are introduced into a square glass capillary (Vitrotubes) with a bottom wall thickness of 100  $\mu\text{m}$ . The capillary is then sealed and placed on the chip. The sealing of the capillary prevents the evaporation of the liquid, thereby suppressing liquid motion within the channel. Figure 4.6 shows the successful displacement of the magnetic microparticles in the system and demonstrates in addition the capability of the system to detect the presence of the particle over the SPAD at the coil center via the microeclipse effect discussed previously. Even though the particle is larger than the coil's center opening, the incident light is not fully blocked, which is in agreement with the projection model based on transit photometry.

### *Particle Size Measurements*

In a second step, smaller particles (1, 3, 5, and 6  $\mu\text{m}$ ) are introduced into the system in order to examine the system's ability to distinguish between the different particle sizes. The glass capillary, used to hold the highly diluted solutions of particles, has a sidewall thickness of 25  $\mu\text{m}$ , which will allow larger magnetic forces and a better resolution than the capillary used in the first experiments, due to the smaller distance between the particle and the sensing element.

Figure 4.7 shows the signal obtained from a SPAD during the transit of the different magnetic particles. The signals for particles of different sizes can be clearly

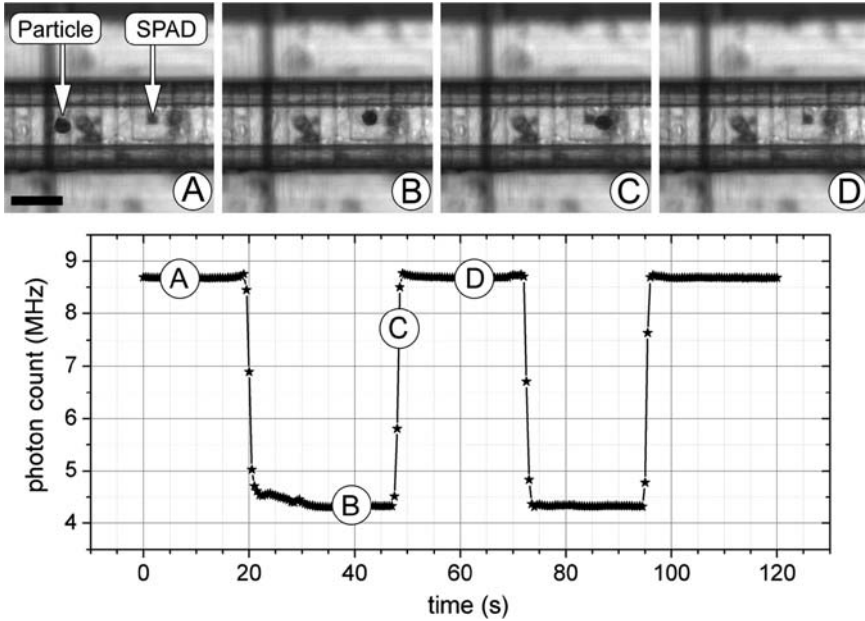


**Fig. 4.6** Sequence of transport of a particle of  $\varnothing = 30 \mu\text{m}$  in a glass capillary with a sidewall  $50 \mu\text{m}$  thick in combination with the corresponding photon count of the indicated SPAD. The particle is held immobile over the coil center during the measurements (*dimension bar*  $100 \mu\text{m}$ )

distinguished, and we see that particles with a diameter as low as  $\varnothing = 1 \mu\text{m}$  can be easily detected by the system. The measurements show an additional effect, which is related to the noncollimated character of the light source. Even though the phenomenon varies between the particle types, we observe that when a particle approaches the SPAD's field of vision, the photon count increases before the expected drop in intensity occurs.

This pretransition peak results from the emission, from the microscope's light source, of light of broad bandwidth and of various angles forming the objective's light cone in combination with the reflection of light falling onto the opaque particle. Thus some photons, which would normally arrive outside the SPAD's sensitive area, are diverted toward the active region and increase the measured photon flux, as schematically shown in Fig. 4.8. The probability for the redirection of photons toward the SPAD center increases as a particle gets closer to the detection area.

However, once a particle fully enters the SPAD's fields of vision, light is no longer diverted toward the SPAD's sensitive area, but away from it, which leads to the previously described effect of the microeclipse. In consequence, the number of photons arriving at the sensor surface is reduced. The evaluation of the measurements for the different particle sizes and their comparison with the model is presented in Fig. 4.9.

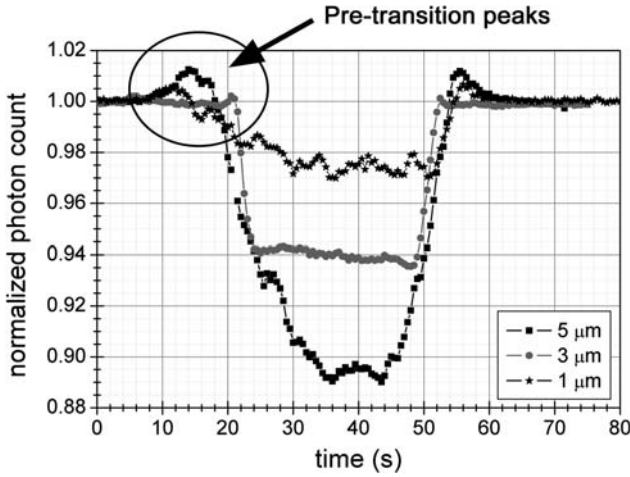


**Fig. 4.7** Normalized photon count of a SPAD during transit of single particles with 1-, 3-, and 5- $\mu\text{m}$  diameter. (Reprinted from Lehmann et al. [10], with permission © 2008 Elsevier)

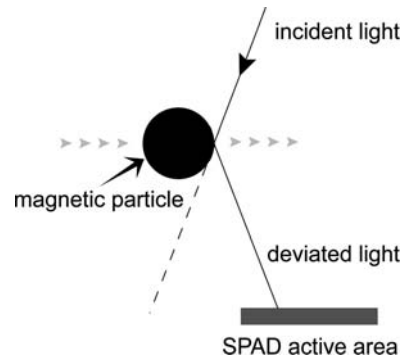


**Fig. 4.8** Schematic of origin of pretransition peak. The incoming magnetic microparticle deviates incident light, arriving out of bounds, toward the SPAD’s sensitive area

We see that the measurements agree well with the expected values and that, as predicted by the model, a small distance between the particles and the sensors favors high resolution. However, observation shows that, for the measurement of larger particles or cells, an increased distance is advantageous, since the upper limit of detection will increase as well. As an example, the calculated maximum diameter of a particle that can be detected in a capillary with a sidewall thickness of  $25\ \mu\text{m}$  is  $\varnothing = 17\ \mu\text{m}$ , while a capillary with a  $100\text{-}\mu\text{m}$ -thick sidewall can detect particles up to  $60\ \mu\text{m}$  in diameter. But we also see that the minimum size of particles that can be detected depends on the width of the capillary wall. While a capillary with a sidewall thickness of  $25\ \mu\text{m}$  allows the detection of particles  $1\ \mu\text{m}$  in diameter, a capillary with a sidewall thickness of  $100\ \mu\text{m}$  will yield the same signal for particles  $5\ \mu\text{m}$  in diameter. Thus the “working distance,” defined by the channel bottom, needs to be chosen as a function of the required resolution and detection limits.

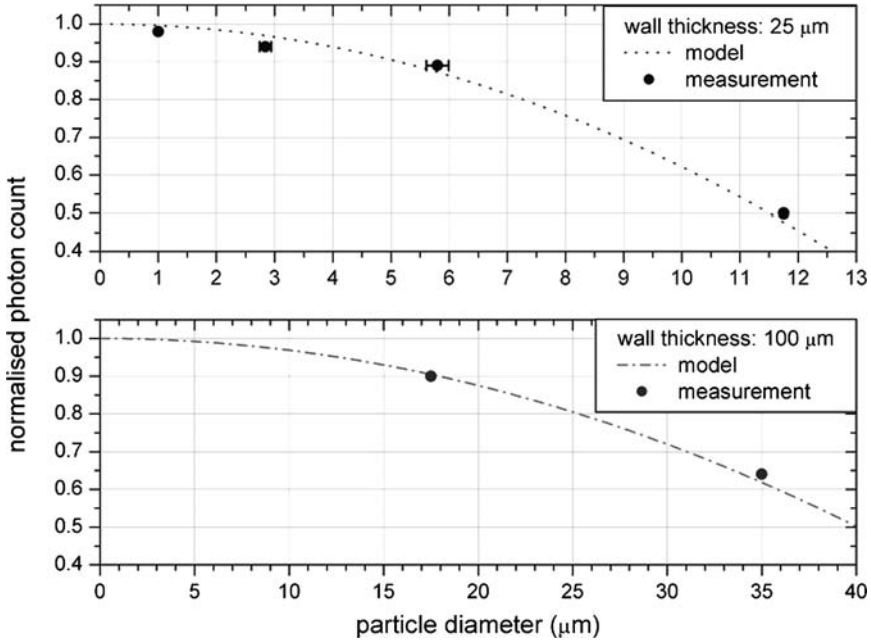


**Fig. 4.9** Comparison of measured and expected values for different particle diameters and varying capillary wall thicknesses. (Reprinted from Lehmann et al. [10], with permission © 2008 Elsevier)

### Particle Velocity Measurements

When recording the signals of two adjacent SPADs simultaneously, we are able to determine the average particle velocity, as Fig. 4.10 demonstrates. During the time elapsed between the intensity drops of two adjacent SPADs, the magnetic particle travels a distance of 200 μm.

The measured average velocity can be translated into the magnetophoretic mobility of the particles based on the theoretical value of the magnetophoretic driving force  $\vec{S}$  in the direction of the particle displacement. Figure 4.11 shows the result of an analytical simulation of the forces along the coil centerline generated by the magnetic actuation. The magnetophoretic driving force  $S$  can be calculated using the law of Biot-Savart:

$$\vec{B} = \frac{\mu_0}{4\pi} I \int \frac{d\vec{l}}{r^2} \times \frac{\vec{r}}{|\vec{r}|}, \tag{4.9}$$

where  $I$  is the current,  $r$  the distance between the wire and the point of interest, and  $d\vec{l}$  the length of the wire section. Since each square coil consists of multiple wire segments of finite length, the field of such a coil can be determined via the superposition of the fields of all segments.

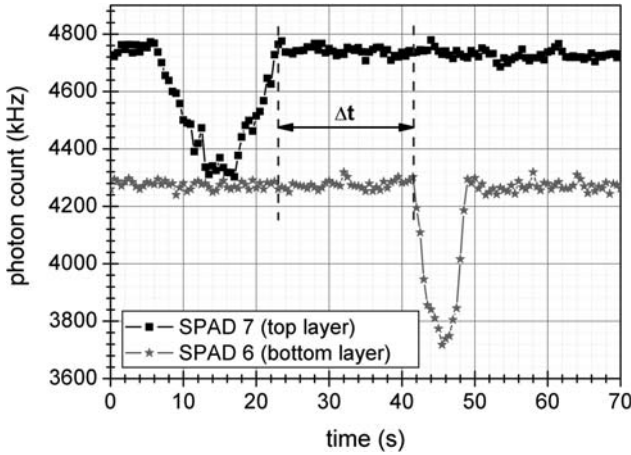


**Fig. 4.10** Photon count of two adjacent SPADs during particle transport for a particle  $5\ \mu\text{m}$  in diameter showing the successive intensity drops. During the time difference  $\Delta t$  the particle moved in a straight line from SPAD 7 to the neighboring SPAD 8. (Reprinted from Lehmann et al. [10], with permission © 2008 Elsevier)

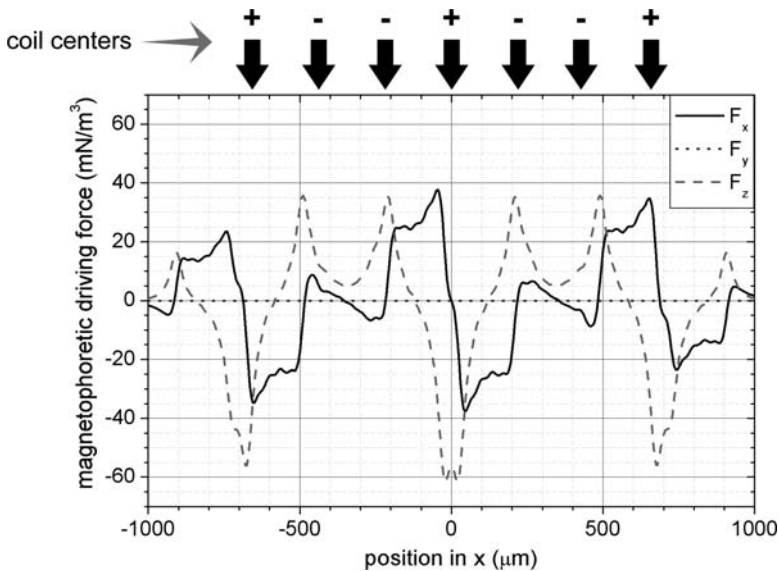


**Fig. 4.11** Analytical simulation of magnetophoretic driving forces in capillary positioned over coil centers ( $y = 0$ ). The arrows indicate the positions of the coil centers, with the algebraic signs identifying the orientation of the local magnetic field

We see that the particles experience a force in the  $x$ -direction directed from the repulsive ( $-$ ) coils to the closest attractive ( $+$ ) coil, while the force in the  $y$ -direction is close to zero. Additionally, the particles experience a repulsive force in the  $z$ -direction at the position of coils carrying negative currents ( $-$ ) but are attracted

**Table 4.1** Summary of average particle velocities for magnetic particles examined in system

$\varnothing(\mu\text{m})$	Magnetite (wt%)	$v(\mu\text{m/s})$	$F_{\text{drag}}$ (fN)	$F_{\text{norm}}$ (kN/m <sup>3</sup> )	$\Delta\chi$
1	63.4	1.6	13.6	35.6	3.3
1.6	42.5	2.9	43.7	20.4	1.9
3	12.5	4.7	124.0	10.8	1.0
6	5.5	5.9	322.5	3.2	0.3

toward the chip when reaching the position of coils carrying positive currents (+). Thus the particles are lifted from the capillary surface and, in consequence, experience a viscous drag during the transport. When reaching the center of the next attractive coil, the particles are again pulled toward the capillary bottom, which ensures a constant distance between particle and SPAD for all optical measurements, depending only on the thickness of the capillary wall.

The comparison of the measured velocities, summarized in Table 4.1, shows a higher average velocity for the larger particles, even though their relative content of magnetically active material is lowest. The particle velocity can be translated into the viscous drag force  $F_{\text{drag}}$  acting on the particle during transport via (4.3). The obtained values are presented in Table 4.1 together with the drag force per unit volume  $F_{\text{norm}}$ .

We see that, while the velocity, and thus the magnetic force acting on the particle, increases with the diameter, the force per unit volume decreases relative to the magnetite content of the particle.

Using the relation for the magnetophoretic mobility (4.8), it is furthermore possible to determine the relative magnetic susceptibility  $\Delta\chi$  of a particle. With the viscosity of the liquid of  $\eta = 1 \text{ mPa s}$  and the average magnetophoretic driving force  $S = 27 \text{ mN/m}^3$ , we obtain the susceptibility values listed in the last column of Table 4.1.

When plotting the calculated relative magnetic susceptibility over the given magnetite content, we see that the magnetic susceptibility of the particles is related to the magnetite content via an exponential function (Fig. 4.12). The measured values also show the superparamagnetic character of the particles, since their relative susceptibility is significantly higher than the values known for paramagnetic materials.

Table 4.1 also demonstrates that the forces obtained by the magnetic actuation are in the fN range. For this reason, the particles can only be held against very low flow rates – on the order of micrometers per second, which makes the current system unsuitable for high flow-through bioanalytical protocols [15, 16]. The introduction of an additional retention system, e.g., via dedicated coils, could solve this problem and thus opens the way toward stop-flow bioanalytical protocols using single magnetic particles or magnetically labeled cells.

However, the system's capability for the optical measurements of particle size and particle velocity will permit determining the magnetic parameters of particles or magnetically labeled cells. Especially in the case of cells, the magnetophoretic mobility can be used as a measure for the number of magnetic particles attached to

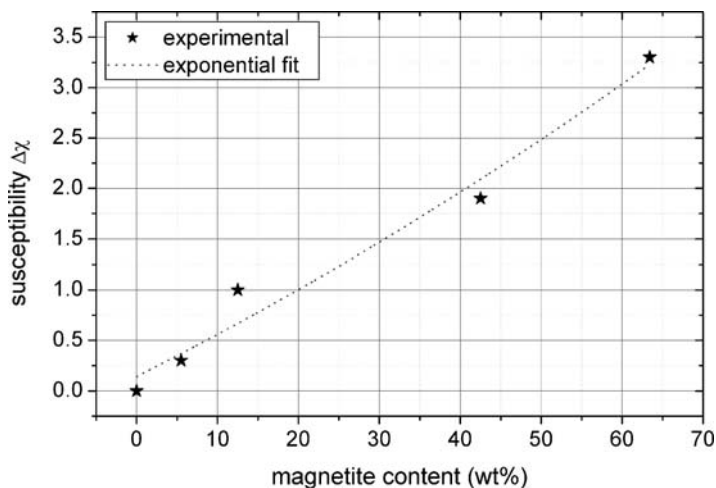


**Fig. 4.12** Magnetic susceptibility  $\Delta\chi$  as obtained from velocity measurements for known particle sizes

the cell surface, which are in turn an indicator for the number of specific binding sites expressed by the cell [17–19].

### *Fluorescent Measurements*

The particle size measurements demonstrate the high sensitivity of the optical detection system, which is able to detect the intensity drop created by the passage of a particle with a diameter of  $1\ \mu\text{m}$ . Additionally, it is known that SPADs are able to perform fluorescent measurements. Thus by replacing the broadband light source with a UV lamp (X-Cite series 120, Zeiss), the system can be easily changed into a configuration for on-chip fluorescent detection. For an efficient fluorescent measurement, it is thus important that the emission wavelength matches the maximum sensitivity of the SPAD.

Based on standard immunoassay protocols (Fig. 4.13), we can envision a LOC that allows the detection of a fluorescent label captured at the surface of a single magnetic particle. In order to test the fluorescent detection principle, we first use nonfluorescent streptavidin-coated magnetic particles  $3\ \mu\text{m}$  in diameter, to whose surface biotinylated antibodies with a fluorescein isothiocyanate (FITC) label can be bound. An estimation of the particles' loading capacity, according to the information given by the supplier, yields  $2.6 \times 10^6$  antibodies that can be bound to the particle surface until saturation point is reached. In terms of total weight, this amount of antibodies corresponds to  $0.6\ \text{pg}$  of bound material.

When a particle that carries fluorescent molecules at its surface approaches the coil center, the photon count at the sensor will drop due to the microeclipse effect,

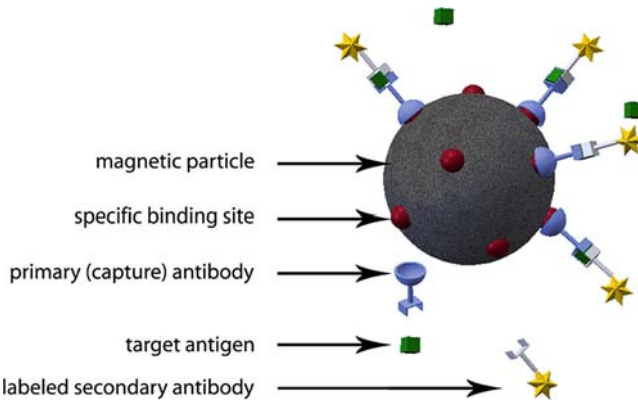


**Fig. 4.13** Schematic of a sandwich immunosorbent assay on a microparticle. Fluorescent labels allow the quantification of the captured sample

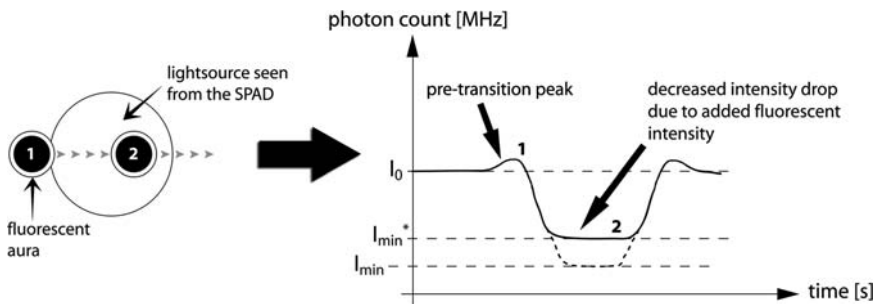


**Fig. 4.14** Principle of fluorescent detection. The fluorescent aura around the particle leads to an increase in the light intensity measured during the microeclipse

but additionally the fluorescent circumference will influence the signal under suitable light conditions. Figure 4.14 demonstrates the case where the system is set to the fluorescence mode. Due to the light emission at the particle’s circumference, the photon count of the SPAD will be higher than in the case of a nonfluorescent particle. The difference between the two signals is the indication for the presence of fluorescent molecules at the particle surface. Such a differential measurement can be performed by varying the wavelength of the light between two measurements on the same particle, which allows recording the microeclipse signal of the same particle with and without the fluorescent component.

The origin of the fluorescent circumference is schematically presented in Fig. 4.15, which depicts how an incident light wave is reflected at the particle surface and is deviated from its path toward the sensor surface. While passing the zone of the fluorescent molecules at the particle surface, the incident or reflected light excites a molecule, which will emit light in any possible direction. Thus a certain fraction of the light emitted in the fluorescently active zone at the particle surface

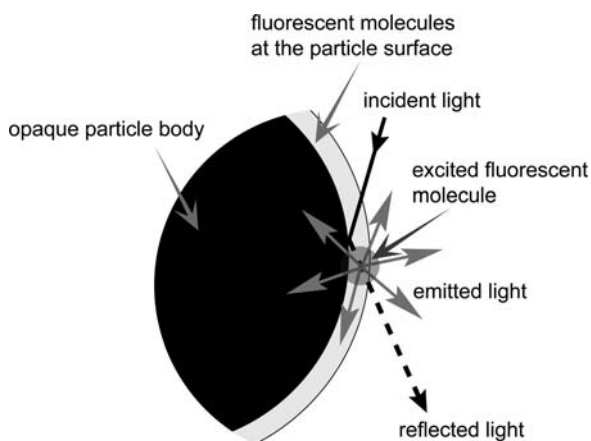


**Fig. 4.15** Schematics of formation of fluorescent aura. The undirected emission of light from molecules excited by blocked or deviated light waves creates an additional light source at the particle circumference

will arrive at the sensor and increase the amount of counted photons. The part of the light-emitting zone “seen” by the SPAD is limited to a stripe along the particle circumference, since the opaque particle body blocks the light emitted at the upper particle hemisphere and prevents the lower hemisphere from being illuminated. In consequence, the measured fluorescent signal does not correspond directly to the total amount of the captured fluorescent molecules but is an indicator of the density of the fluorescent molecules at the particle surface, since a decrease in density will result in a smaller number of active molecules at the particle’s circumference. For example, the density of antibodies at the surface of a fully saturated particle  $3\ \mu\text{m}$  in diameter amounts to  $8.6 \times 10^4$  molecules/ $\mu\text{m}^2$ , which presents the upper limit of detection.

Figure 4.16 shows the SPAD signals of a fully saturated particle illuminated at the excitation wavelength, resulting in a fluorescent emission, and at a different wavelength, resulting in a nonfluorescent microeclipse signal. The drop in the photon count is significantly smaller when the fluorescent emission occurs, which indicates the expected presence of an additional photon source. We further notice that the pretransition peaks observed for the broadband light source also occur during the fluorescent measurements but are clearly smaller than the signal change observed in the experiments employing a broadband light source.

Measurements show that the difference between the nonfluorescent particle and the particle fully covered with fluorescent molecules is on average 66% of the total signal change, which is equivalent to the maximum density of bound antibodies and therefore stands for the maximum fluorescent signal.

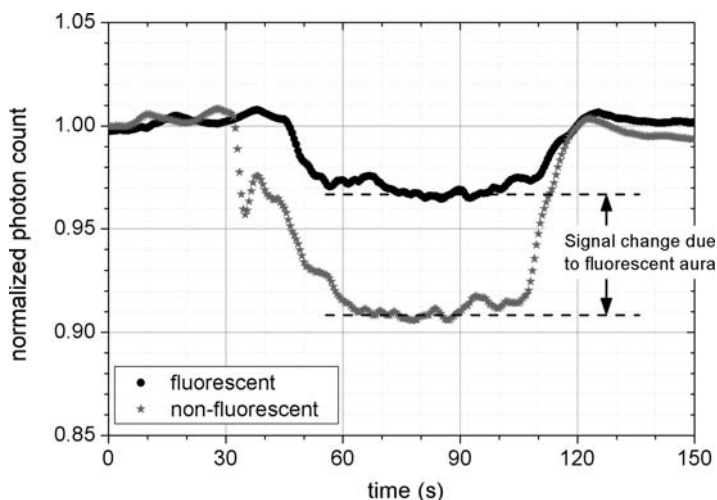


**Fig. 4.16** Measured SPAD signal for a 3- $\mu\text{m}$  particle at excitation wavelength (fluorescent) and at a nonexciting wavelength (nonfluorescent)

### *Bioanalytical Experiments*

In a subsequent development, we look for a correlation between varying concentrations of the target antigen in a sandwich immunoassay protocol (Fig. 4.13) and the differential signal readout from the SPAD. Beads with a mean diameter of 2.9  $\mu\text{m}$  (Bangs Labs) are used as mobile substrate. These beads are coated with streptavidin. A first capture antibody is grafted to the beads, by mixing for 10 min 10  $\mu\text{l}$  of beads, diluted in 100  $\mu\text{l}$  of immobilization buffer, with 100  $\mu\text{l}$  of high-concentration (50  $\mu\text{g}/\text{ml}$ ), biotinylated, polyclonal rabbit antimouse IgG (Dako). Then, beads are retained by means of a magnet and washed for 30 s in 500  $\mu\text{l}$  of a phosphate buffer saline–bovine serum albumin (PBS–BSA) solution. The next step is mixing for 10 min the beads with 100  $\mu\text{l}$  of solution in which different concentrations of the target antigen (the analyte) are dissolved. After a washing step with PBS–BSA, a further step consists in mixing for 10 min the functionalized beads with 100  $\mu\text{l}$  of solution at 167  $\mu\text{g}/\text{ml}$  of Cy3 conjugated affinity purified goat antimouse IgG (Rockland). The last step is washing the beads three times in PBS–BSA solution (500  $\mu\text{l}$  each time).

When reducing the target antigen concentration, the coverage of bound fluorescent labels is reduced, leading to a decrease in the fluorescent signal, as Fig. 4.17 clearly shows. Antigen concentrations above 100  $\text{ng}/\text{ml}$  lead to a saturation of the response. This result indicates that the particle is fully covered by the sample molecules at this concentration. The results obtained for lower concentrations clearly show the expected decrease in the fluorescent signal. The high sensitivity of the SPADs allows us to detect concentrations as low as 66  $\text{pg}/\text{ml}$  of analyte.

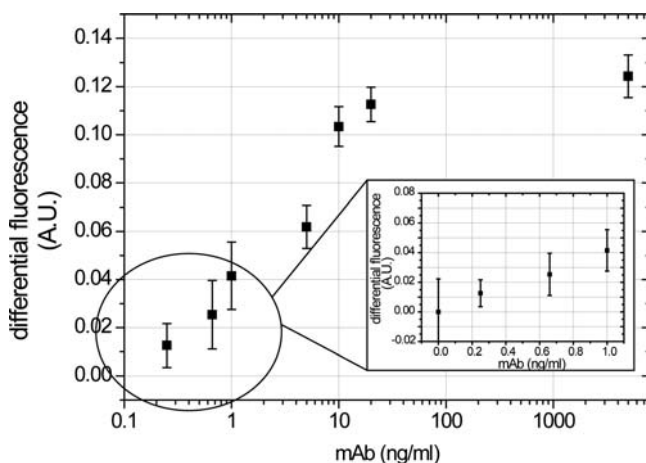


**Fig. 4.17** Measurement of differential fluorescent signal for different concentrations of the IgG monoclonal antibody (mAb) that is the target antigen of our test. The *error bars* indicate the variability in fluorescent response for different magnetic beads

A further remaining challenge is the incubation of the magnetic particles on-chip and performing the sandwich immunoassay fully on-chip. Indeed, the measurements presented above have all been performed using particles prepared and incubated off-chip. Since this type of procedure still requires larger amounts of particles and reagents than actually needed for the on-chip detection, the successful demonstration of the fluorescent detection capabilities of the magneto-optical CMOS system will logically be combined with on-chip retention and manipulation schemes for the magnetic microparticles.

## Conclusion

This chapter successfully demonstrated the capabilities of a magneto-optical CMOS microsystem for the on-chip detection of biological molecules. Our results show the potential of such a system with respect to on-chip bioanalysis. We were able to show that a miniaturized magnetic transport system could be combined with highly sensitive optical detectors, which allows the direct link between magnetic actuation and nonconfocal optical detection. The high sensitivity of the detection allows a differentiation between objects of different sizes as well as varying load of fluorescent molecules. Since it is equally possible to measure the velocity of transport between the detection sites, the magnetic properties of the handled objects can be determined as well. In summary, our magneto-optical CMOS system presents a promising and innovative approach to the design of highly sensitive and flexible bioanalytical microsystems and is anticipated to be able to handle and detect a wide range of biomolecules and cells.

## References

1. Gijs MAM (2004) Magnetic bead handling on-chip: new opportunities for analytical applications. *Microfluid Nanofluidics* 1:22–40
2. Pankhurst QA, Connolly J, Jones SK, Dobson J (2003) Applications of magnetic nanoparticles in biomedicine. *J Phys D Appl Phys* 36:R167–R181
3. Pamme N (2006) Magnetism and microfluidics. *Lab Chip* 6:24–38
4. Landfester K, Ramirez LP (2003) Encapsulated magnetite particles for biomedical application. *J Phys Condens Matter* 15:S1345–S1361
5. Bergemann C, Muller-Schulte D, Oster J, Brassard L, Lubbe AS (1999) Magnetic ion-exchange nano- and microparticles for medical, biochemical and molecular biological applications. *J Magn Magn Mater* 194:45–52
6. Grüttner C, Rudershausen S, Teller J (2001) Improved properties of magnetic particles by combination of different polymer materials as particle matrix. *J Magn Magn Mater* 225:1–7
7. LesliePelecky DL, Rieke RD (1996) Magnetic properties of nanostructured materials. *Chem Mater* 8:1770–1783
8. Zborowski M, Sun LP, Moore LR, Williams PS, Chalmers JJ (1999) Continuous cell separation using novel magnetic quadrupole flow sorter. *J Magn Magn Mater* 194:224–230
9. White FM (1999) *Fluid mechanics*. McGraw-Hill, New York
10. Lehmann U, Sergio M, Pietrocola S, Dupont E, Niclass C, Gijs MAM, Charbon E (2008) Microparticle photometry in a CMOS microsystem combining magnetic actuation and in-situ optical detection. *Sens Actuators B Chem* 132:411–417
11. Lehmann U, Sergio M, Pietrocola S, Niclass C, Charbon E, Gijs MAM (2007) A CMOS microsystem for the integrated actuation and optical detection of magnetic microparticles. The 14th International Conference on Solid-State Sensors, Actuators and Microsystems, Transducers'07 and Eurosensors XXI, pp U1255–U1256, Lyon, France
12. Lehmann U, Sergio M, Pietrocola S, Niclass C, Gijs MAM, Charbon E (2007) Particle shadow tracking – combining magnetic particle manipulation with in-situ optical detection in a CMOS system. The 11th International Conference on Miniaturized Systems for Chemistry and Life Sciences,  $\mu$ TAS 2007 Conference, pp 1179–1181, Paris, France
13. Niclass C, Sergio M, Charbon E (2006) A single photon avalanche diode array fabricated in 0.35  $\mu$ m CMOS and based on an event-driven readout for TCSPC experiments. Conference on Advanced Photon Counting Techniques, pp U216–U227, Boston, MA
14. Rida A, Fernandez V, Gijs MAM (2003) Long-range transport of magnetic microbeads using simple planar coils placed in a uniform magnetostatic field. *Appl Phys Lett* 83:2396–2398
15. Lacharme F, Vandevyver C, Gijs MAM (2008) Magnetic bead retention device for full on-chip sandwich immuno-assay. 21st IEEE International Conference on Micro Electro Mechanical Systems MEMS 2008, pp 184–187, Tucson, AZ, USA
16. Lacharme F, Vandevyver C, Gijs MAM (2008) Full on-chip nanoliter immunoassay by geometrical magnetic trapping of nanoparticle chains. *Anal Chem* 80:2905–2910
17. Yi CQ, Li CW, Ji SL, Yang MS (2006) Microfluidics technology for manipulation and analysis of biological cells. *Anal Chim Acta* 560:1–23
18. McCloskey KE, Chalmers JJ, Zborowski M (2003) Magnetic cell separation: characterization of magnetophoretic mobility. *Anal Chem* 75:6868–6874
19. McCloskey KE, Moore LR, Hoyos M, Rodriguez A, Chalmers JJ, Zborowski M (2003) Magnetophoretic cell sorting is a function of antibody binding capacity. *Biotechnol Prog* 19:899–907